LAMINAR FLOW, STABILITY AND TRANSITION IN HELICAL PIPES

Riccardo Casali, Isa Mammadli*
Institute of Fluid Mechanics (LSTM)
Friedrich–Alexander–Universität (FAU)
91058 Erlangen–Nürnberg, Germany
{riccardo.casali, isa.mammadli}@fau.de

Valerio Lupi
Gran Sasso Science Institute (GSSI)
67100 L'Aquila, Italy
valerio.lupi@gssi.it

Philipp Schlatter
Institute of Fluid Mechanics (LSTM)
Friedrich–Alexander–Universität (FAU)
91058 Erlangen–Nürnberg, Germany
philipp.schlatter@fau.de

ABSTRACT
Helical pipe flow finds applications in several fields, among which heat exchangers, chemical reactors, pipelines and even biological systems, since the the aortic arch can be modelled as a bent pipe. The understanding of the flow characteristics in helical pipes can therefore allow to understand the physics at the basis of a great number of practical applications, as a helix being the representative of many real design geometries. Therefore, in this work we study the laminar flow, its instability and the transition to turbulence with a two-dimensional (2D) steady-state and instability solver, 3D direct numerical simulations (DNS) in full and perturbation mode. First, a validation of the driving force used in the literature is carried out, by comparing our 2D solver with cases where inflow-outflow boundary conditions were used. Furthermore, a validation of the computed 2D eigenmodes with respect to the results of the 3D linearised Navier–Stokes analysis is performed. The dependence of the laminar base flow on the geometric parameters (curvature and torsion) is analysed in detail. Combining the base flow and stability analysis, the critical Reynolds number could be computed with a high accuracy, by means of a continuation method allowing to follow the neutral curve for each helical pipe geometry. The stability results generally show a good agreement with the unique literature work, but some remarkable differences are also identified.
* both authors contributed equally to the work.

INTRODUCTION
Stability, transition and turbulence are well-studied topics in pipe flow, going back to the seminal studies by Osborne Reynolds. However, for straight pipes, only recently a fairly complete picture has emerged (Avila *et al.*, 2023), clarifying the subcritical nature of transition to turbulence. Going from straight to bent pipes, Lupi *et al.* (2024) could show that even (very) low curvatures lead to a modal instability, although the supercritical nature of transition becomes dominant only above a certain curvature radius (Canton *et al.*, 2020). Modal stability of helical pipe flows has only been considered in the study by Gelfgat (2020) (and follow-up papers). However, only a BiGlobal linear stability analysis has been performed, using comparably low-order numerical schemes, without a thorough three-dimensional validation.

Given the limited available data for helically bent pipes, we initiated the current work to address some of the identified research gaps, including a detailed characterisation of the (steady) laminar flow in helical pipes (see Canton *et al.* (2017) for the corresponding toroidal flows), linear modal and non-modal stability, and turbulent flows. For this purpose, we have implemented a novel code for two-dimensional stability in a helical coordinate system and ported a periodic method to simulate laminar and fully turbulent helical pipe flows on modern GPU-based systems (Jansson *et al.*, 2024).

METHODOLOGY
Pipe geometry and coordinate system
The geometry is characterised by the pipe radius R_p, curvature radius R_c and the pitch p_s, being $2\pi p_s$ the elevation of one revolution of the helix (see Figure 1). The values can be put together to form the nondimensional curvature δ and torsion τ parameters,

$$\delta = \frac{R_c R_p}{R_c^2 + p_s^2}\,, \quad \tau = \frac{p_s R_p}{R_c^2 + p_s^2}\,. \tag{1}$$

In order to compare the stability results with Gelfgat (2020), the torsion-to-curvature ratio λ is defined as $\lambda = \tau/\delta$. It can be shown that the length of the centerline for one full revolution of the helix is $l_{rev} = 2\pi\sqrt{R_c^2 + p_s^2}$. It should be noted that for some (δ, τ) (see *e.g.* Figure 5) the low pitch causes the physical pipe to intersect itself. The orthogonal helical coordinate system from Germano (1982) is adopted, with Lamé coefficients defined as

$$h_s = 1 + \delta r \sin(\theta + \phi), \quad h_r = 1, \quad h_\theta = r\,. \tag{2}$$

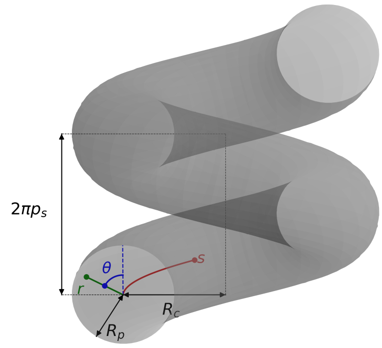

Figure 1. Sketch of the helical pipe geometry, showing the pipe cross-sectional radius R_p, radius of curvature centreline R_c, and pitch p_s. The helical coordinate system with radial (r), azimuthal (θ), and streamwise (s) coordinates is shown.

Base flow computation

To compute the steady base flow $Q = \{U, P\}$, with U being the velocity vector and P the pressure, a two-dimensional (2D) steady-state solver (described in Casali, 2025) is implemented. Due to its streamwise invariance, the base flow is computed on a cross-section of the helical pipe. A spectral collocation method is used for the spatial discretisation, employing Fourier and Chebyshev basis functions in the azimuthal and radial directions, respectively.

The computation of the steady base flow requires the numerical approximation of the steady incompressible Navier–Stokes equations, which in non-dimensional form read

$$\begin{aligned} &(U \cdot \nabla)U + \nabla P - \frac{1}{Re}\nabla^2 U - f = 0, \\ &\nabla \cdot U = 0 \,, \end{aligned} \tag{3}$$

where Re is the Reynolds number based on the pipe diameter and the bulk velocity U_b, i.e. $Re = 2R_p\, U_b/\nu$, and f is a volume force driving the flow, defined as (Kumar, 2020)

$$f = \frac{F}{h_s} e_s \,, \tag{4}$$

where the forcing amplitude F is the equivalent of the streamwise pressure gradient $\partial p/\partial s$ and e_s is the unit vector in the streamwise direction. The equations are written in the orthogonal helical coordinate system (Germano, 1982; Hüttl *et al.*, 1999) introduced above, and no-slip boundary conditions are applied at the wall.

The system (3) is augmented with a constraint on the bulk velocity, $U_b(f) = 1$, which provides the forcing amplitude F, and with equations to cancel out the spurious pressure modes. The solution is then obtained through the Newton–Raphson method coupled with a continuation algorithm in Re, δ, τ, starting from the Stokes solution as initial guess.

Modal stability analysis

Hydrodynamic stability is investigated through modal stability analysis (Schmid & Henningson, 2001; Drazin & Reid, 2004), *i.e.* by studying the evolution of infinitesimal perturbations $q' = \{u', p'\}$ on top of the steady base flow Q. This evolution is governed by the incompressible Navier–Stokes equations linearised around the basic state,

$$\begin{aligned} &\frac{\partial u'}{\partial t} + (U \cdot \nabla)u' + (u' \cdot \nabla)U + \nabla p' - \frac{1}{Re}\nabla^2 u' = 0, \\ &\nabla \cdot u' = 0 \,. \end{aligned} \tag{5}$$

The perturbations are considered periodic in the streamwise direction s and in time t, so that through a Fourier transform they assume the form (normal modes ansatz)

$$q'(s, r, \theta, t) = \sum_{\alpha=-\infty}^{+\infty} \hat{q}_\alpha(r, \theta) e^{\,\mu t + i\alpha s} \,, \tag{6}$$

where $\alpha = 2\pi R_p / l_s$ is the streamwise wavenumber, being l_s the wavelength, and $\mu = \sigma + i\omega$ is the complex eigenvalue.

For each streamwise wavenumber, one obtains the following eigenvalue problem

$$-\mu \mathscr{M} \hat{q}_\alpha = \mathscr{L} \hat{q}_\alpha \,, \tag{7}$$

where $\mathscr{M}$ is the mass matrix and $\mathscr{L}$ the linearised Navier–Stokes operator, defined as

$$\mathscr{M} = \begin{pmatrix} \mathscr{I} & 0 \\ 0 & 0 \end{pmatrix}, \quad \mathscr{L} = \begin{pmatrix} \nabla_0 U + U \cdot \nabla_\alpha - \frac{1}{Re}\nabla_\alpha^2 & \nabla_\alpha \\ \nabla \cdot_\alpha & 0 \end{pmatrix} \,, \tag{8}$$

where $\mathscr{I}$ is the 3×3 identity matrix and ∇_α is used to emphasize that the differential operators depend on the wavenumber α, since the term $e^{i\alpha s}$ contributes to $\partial/\partial s$, as described in Casali (2025). Solving the eigenvalue problem (7), we find that the base flow U is (modally) stable when the real part of the eigenvalue is negative, *i.e.* $\sigma < 0$.

In order to obtain the critical Reynolds number for each geometry, *i.e.* a combination of δ and τ, a two-step procedure is adopted. First, a secant method in Re at fixed α is employed to reach the neutral curve (Re, α), using α from the computations of Gelfgat (2020). For a new geometry, it would be necessary to try different α values and take the one with lower Re_{cr}. To follow the neutral curve, a continuation algorithm is implemented (Casali, 2025), allowing to determine Re_{cr} with at least 0.1% accuracy, α_{cr} and ω_{cr} with at least 1% accuracy, given the adopted tolerances.

When dealing with non-dimensionalisation, three kinds of quantities, *e.g.* length L, play a role: physical quantities $\tilde{\cdot}$, reference physical quantities $\cdot^0$, and non-dimensional quantities $\cdot = \tilde{\cdot}/\cdot^0$. This matters in particular for pipes where both non-dimensionalisation with R_p^0 or $D_p^0 = 2R_p^0$ can be performed. It is straightforward that $Re_D = D_p^0 U_b^0/\nu^0 = 2Re_R$, *i.e.* the Reynolds number based on the diameter ($L^0 = D_p^0$) is the double of the one based on radius ($L^0 = R_p^0$). To derive the same relation for α and μ, it is necessary to recall that the physical wavelength is $\tilde{l}_s = L^0 2\pi/\alpha$. Then one has $\tilde{l}_s = R_p^0 2\pi/\alpha_R = 2R_p^0 2\pi/\alpha_D \implies \alpha_R = \alpha_D/2$. With the same reasoning for the physical time L^0/U^0, it is easy to show that $\mu_R = \mu_D/2$.

Three-dimensional linear and non-linear DNS

To validate the computations of the 2D base flow, non-linear direct numerical simulations (DNS) of the flow in a suf-

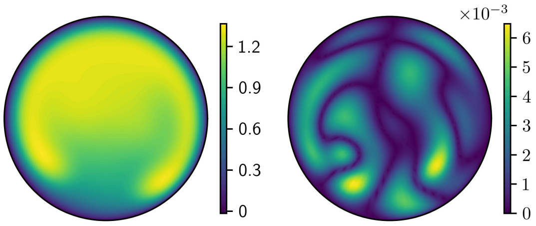

Figure 2. *Left:* Mean flow and *right:* error ε between 2D computations and 3D non-linear DNS for $\delta = 0.65$, $\tau = 0.3$ and $Re = 500$ at $N_{rev} = 3.30$ ($s = 14.5$).

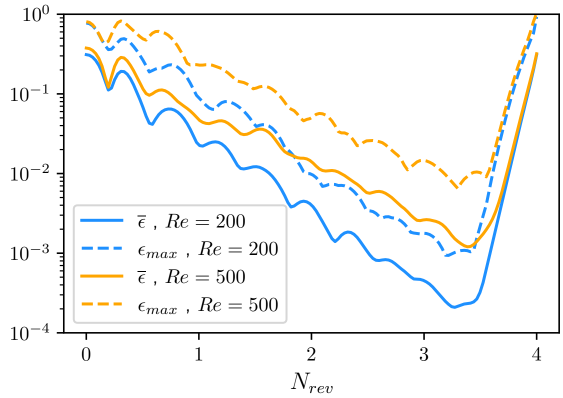

Figure 3. Average $\overline{\varepsilon}$ and maximum ε_{max} error between 2D computations and DNS with $\delta = 0.65$ and $\tau = 0.3$ with respect to the turns N_{rev} along the streamwise coordinate.

ficiently long helical pipe are carried out using Neko (Jansson *et al.*, 2024). This framework solves the incompressible Navier–Stokes equations in the Cartesian coordinate system employing the spectral element method (SEM). The domain is discretised into non-overlapping hexahedral elements and the solution is represented on local elements with N^{th}-order Legendre polynomials interpolated on Gauss–Lobatto–Legendre (GLL) nodes. The same interpolants are used for velocity and pressure, corresponding to the $P_N - P_N$ formulation. The integration in time relies on a semi-implicit BDF3/EXT3 scheme: the equations are discretised with a third-order backward differentiation formula (BDF3), and an extrapolation scheme of order three is applied to the non-linear term at the new time step.

The Hagen–Poiseuille velocity profile is prescribed at the inlet, whereas a stress-free boundary condition is imposed at the outlet and no-slip boundary conditions are applied at the wall. A parabolic velocity profile in the streamwise direction is used as the initial condition. The length of the pipe is chosen as $s_f = 4l_{rev}$. The transient simulations are run until no noticeable differences are observed in the flow fields. The resulting fields are interpolated onto the same mesh as that used to compute the 2D base flow and transformed into helical coordinates for pointwise comparison.

To validate the unstable eigenmodes computations, we also consider the linearised Navier–Stokes equations (5), solved using the spectral-element code Nek5000 (Fischer *et al.*, 2025). In this case, a staggered grid is employed ($P_N - P_{N-2}$), in which the pressure is represented with Lagrangian basis functions of order $N-2$ defined on Gauss–Legendre points. The two-dimensional base flow computed with our steady-state solver is interpolated on the SEM mesh and transformed to Cartesian coordinates. The perturbation velocities are initialised as a white noise. Periodic boundary conditions are imposed in the streamwise direction, while homogeneous Dirichlet boundary conditions are prescribed at the wall. The kinetic energy of the perturbations is calculated as

$$E_k = \int_V \frac{1}{2}(u')^2 \mathrm{d}V \ , \tag{9}$$

where V is the volume of the pipe section.

RESULTS

Validation of the forcing

In order to validate the correctness of the forcing formulation, both from a numerical and a physical point of view, a pointwise comparison of the 2D base flow with the 3D non-linear inflow–outflow DNS is performed. It is important to underline that in the DNS the flow is purely driven by the inflow boundary conditions (*i.e.* its mass flow), therefore the forcing is absent: the comparison between the two solutions allows one to validate the forcing technique here implemented also from a physical perspective.

The geometry chosen has high curvature and medium torsion, *i.e.* $\delta = 0.65$ and $\tau = 0.3$. Two different values of the Reynolds number are analysed, $Re = 200$ and $Re = 500$.

Figure 2 presents the pointwise difference $\varepsilon = u_s^{2D} - u_s^{DNS}$ for the velocity components and pressure between the 2D calculation and the 3D non-linear DNS at $Re = 500$. The cross-section at $N_{rev} = s/l_{rev} = 3.3$ is shown, where the error is minimum. Figure 3 shows the average error $\overline{\varepsilon}$ over the grid points and the maximum error ε_{max} over the cross-section for both values of the Reynolds number. The maximum error is below 1% for $Re = 500$ and below 0.1% at $Re = 200$. The average error is about one order of magnitude lower for both cases. The better accuracy at lower Re is due to the fact that the two DNS do not reach the fully developed state, because of the finite pipe length. This is visible from the fact that the error lowers along s with a monotone fashion, despite the bumpy behaviour, with a linear trend in logarithmic scale, as can be seen in Figure 3. The sudden increase at the end of the pipe is due to the outflow boundary condition. Therefore, it could also be concluded that the required pipe length to reach the fully-developed state increases with Re, at least for the considered geometry.

It should also be noted that the error contours of Figure 2 is quite irregular. This result, along with the awareness that the errors would further decrease exponentially by increasing the pipe length, allows us to conclude that both the forcing formulation and the numerical computation of the base flow are correct.

Base flow characterisation

For straight pipes, where the wall shear stress τ_w is uniform over the surface, the skin friction factor, also called *Fanning friction factor*, is defined as

$$C_f = \frac{\tau_w}{\frac{1}{2}\rho U_b^2} \ , \tag{10}$$

where ρ is the density of the fluid.

The Darcy friction factor f_D is a quantity strictly related to the Fanning friction factor, being for a straight pipe with

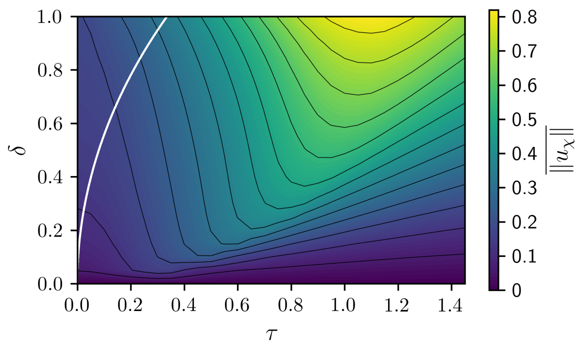

Figure 4. Mean secondary flow velocity magnitude $\overline{\|u_\chi\|}$ at $Re = 400$, as a function of curvature δ and torsion τ. Isolines of $\overline{\|u_\chi\|}$ are shown in black. The region where the helical pipe intersects itself is located to the left of the white line.

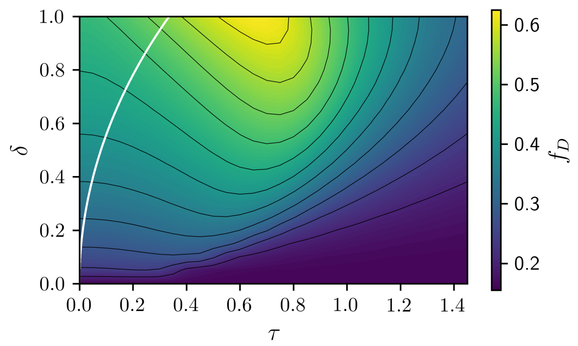

Figure 5. Darcy friction factor f_D at $Re = 400$, with respect to pipe curvature δ and torsion τ. f_D isolines in black. At the left of the white line is the region where the pipe intersects itself.

laminar flow:

$$f_D = \frac{64}{Re_D}, \qquad \tau_w = \frac{1}{8} f_D \rho U_b^2 \implies f_D = 4C_f \tag{11}$$

In a straight pipe, the Fanning friction factor is defined as

$$C_f = \frac{R_p}{\rho U_b^2} \frac{\mathrm{d}p}{\mathrm{d}s} \, . \tag{12}$$

In a helical pipe, the streamwise pressure gradient is equivalent to the forcing constant, therefore the Darcy friction factor can be computed as $f_D = 4F$, with the non-dimensional forcing amplitude.

Laminar flows in bent pipes are characterised by a non-parabolic streamwise velocity profile and a secondary flow in the radial and azimuthal directions (Casali, 2025). In particular, in the toroidal geometry, it presents two perfectly symmetric vortices with respect to the equatorial plane of the torus, named after Dean (1927). Going from the toroidal to the helical geometry, the non-zero torsion causes the breaking of the symmetry at first, with the vortex rotating in the opposite direction of the torsion (obtaining through the right-hand rule around the tangent unitary vector) that shrinks progressively as the torsion is further increased. To investigate the strength of the secondary motion, the secondary flow velocity vector is defined as

$$u_\chi = (0, u_r, u_\theta) \, , \tag{13}$$

and the mean norm is chosen as a representative quantity

$$\overline{\|u_\chi\|} = \frac{1}{A} \int_A \|u_\chi\| \mathrm{d}A = \frac{1}{A} \int_A \sqrt{u_r^2 + u_\theta^2} \, \mathrm{d}A \, , \tag{14}$$

where A is the cross-sectional area of the pipe. The basic states are computed at $Re = 400$, for which the flow would be laminar also in nature for almost every geometry computed, according to Gelfgat (2020) and Casali (2025). Computations at $Re = 200$ are also performed, showing the same qualitative features. Regarding the geometric parameters, $\delta \in (0, 1]$ and $\tau \in [0, 1.45]$, with values separated by steps of 0.05. The value $\delta = 0$ is not considered, as it represents the straight pipe, where the secondary flow is absent.

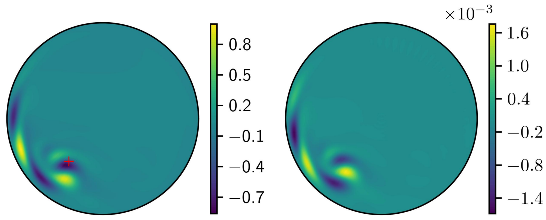

Figure 6. Computed eigenmode (left) and pointwise difference (right) for the 2D streamwise perturbation u_s' between the 2D code and Nek5000. The red plus symbol indicates the probe location used in Figure 8.

The magnitude of the secondary flow is shown in figure 4. At fixed torsion, its value increases monotonically with δ. This behaviour can be expected since the importance of the Dean vortices increases with curvature. It is interesting to observe that, at fixed curvature, $\overline{\|u_\chi\|}$ first increases with τ, then a clear maximum is reached, in particular in the upper region where the global maximum for $(\delta, \tau) = (1, 1)$ is visible, and then decreases as the torsion is further increased. The friction factor is shown in Figure 5. One can directly see that it closely follows the behaviour of the secondary flow intensity. This finding suggests a correlation between $\overline{\|u_\chi\|}$ and f_D. Indeed, to drive the secondary flow, more energy is required, which can only come from the pressure gradient, and this translates to a higher friction factor.

Validation of the eigenmodes

In order to validate the computation of the most unstable eigenmode, a comparison with the 3D perturbation formulation is performed. The chosen geometry has $\delta = 0.1$ and $\tau = 0.1$, since a deviation from the results of Gelfgat (2020) is found for this case. In order to have a growing perturbation, a slightly supercritical case ($Re = 3000$) is considered. The initial perturbation in the 3D simulations is set as white noise with arbitrary amplitude, and the length of the domain is taken equal to the wavelength of the (expected) most unstable eigenmode, $s_f = l_s$.

Figure 6 shows the streamwise velocity component u_s' of the computed eigenmode and the pointwise difference between the two methods, which is of the order of 10^{-3}. The kinetic energy E_k of the perturbations (see equation (9)) is displayed in

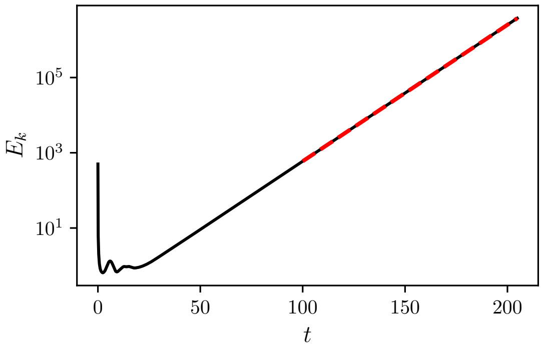

Figure 7. Time evolution of the kinetic energy E_k (black) of the perturbation from the linearized Navier–Stokes simulations in Nek5000. The straight line fit (red) is used to compute the growth rate σ.

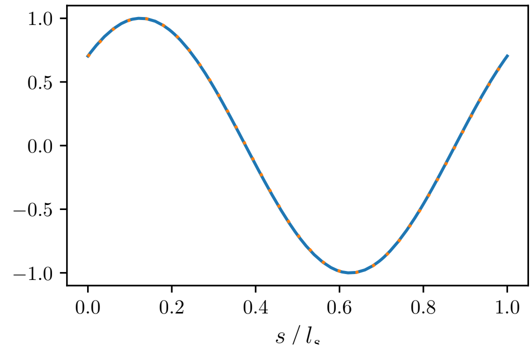

Figure 8. Normalized streamwise velocity component $\hat{u}_s/\max_s \hat{u}_s$ with respect to s/l_s, sampled at $r = 0.573$ and $\theta + \phi = -2.242$ at time 200. The orange points correspond to a sinusoidal function fit to the data.

Figure 7 as a function of time. The fitted straight line (red) produced the slope of $\mathrm{d}(\ln E_k)/\mathrm{d}t = 1/E_k \int_V \mathrm{d}/\mathrm{d}t(1/2(u')^2)\mathrm{d}V = 2\sigma = 0.083535$ (using the ansatz $u' = \mathrm{Re}(\hat{u}_\alpha(r,\theta)e^{\mu t}e^{i\alpha s})$, while the growth rate computed with the 2D stability code gives $2\sigma = 0.083544$. Hence, this agreement confirms the accuracy of our method. In figure 8 the normalised streamwise velocity component $u_s/\max_s u_s$ with respect to s, sampled at $(r,\ \theta+\phi) = (0.573,\ -2.242)$ is shown. One period of a sinusoidal function is obtained, as expected. This also proves the correctness of the scaling discussed in the previous section.

Neutral curves

Besides the base flow computation, a modal stability analysis is also performed, aimed at comparing to the data reported by Gelfgat (2020) and determining whether the two numerical methods used (finite differences and spectral) lead to the same results.

Each geometry, characterised by the curvature δ and torsion-to-curvature ratio λ, is described by a different base flow, causing the transition to turbulence to happen at very different Reynolds numbers, as can be seen from Figure 9. The geometries with $\lambda = 0$ correspond to toroidal pipes, and have already been validated with the results provided by Canton *et al.* (2016). As can be seen from the graph, the results at low values of λ (low torsion), show very good agreement with the reference data for all curvatures. The same, except for a bias for $\delta = 0.01$, can be stated for high λ values. For inter-

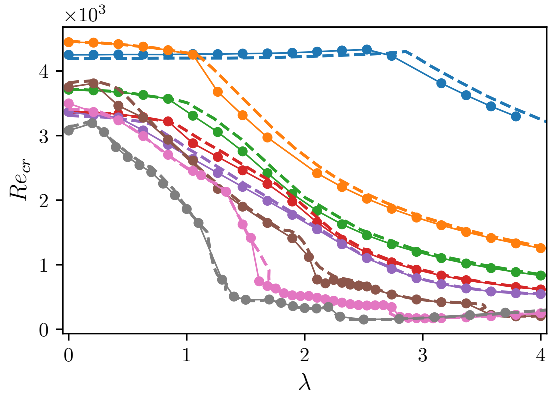

Figure 9. Critical Reynolds number (filled circles) compared to literature results by Gelfgat (2020) (dashed). Legend in figure 11.

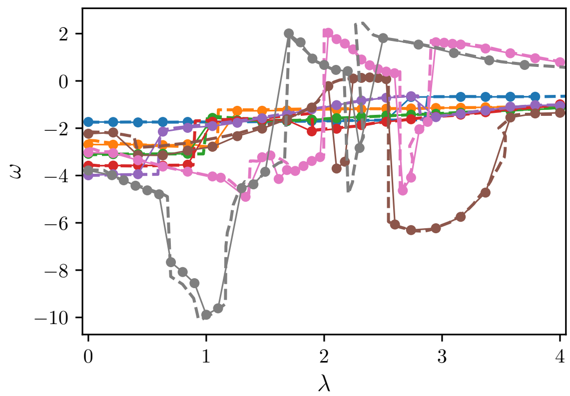

Figure 10. Frequency of marginally stable modes (filled circles) compared to literature results by Gelfgat (2020) (dashed). Legend in figure 11.

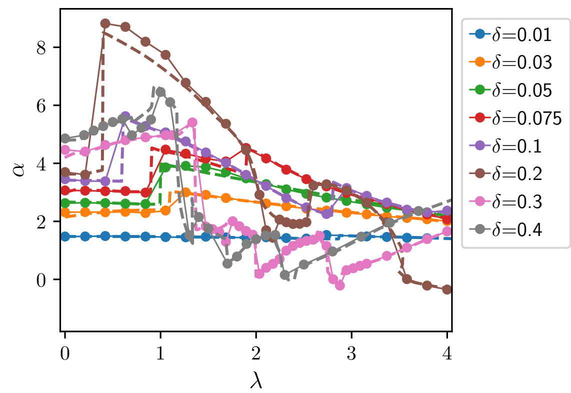

Figure 11. Axial wavenumber of marginally stable modes (filled circles) compared to literature results by Gelfgat (2020) (dashed).

mediate torsion values, however, larger differences in Re_{cr} are found. It is worth mentioning that, except for the lowest curvature value, the critical Reynolds number found in the present work is always lower than that obtained by Gelfgat (2020). It is then likely that the discretisation in α and ω carried out by Gelfgat (2020) was too rough, or that the present computations, with an accurate spectral resolution, allow some new

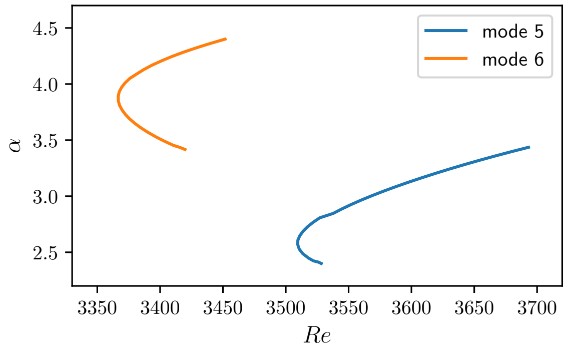

Figure 12. Neutral curves of modes 5 and 6 (Casali, 2025) for $\delta = 0.05$, $\lambda = 1$.

base flow or modal features to be represented by the discretisation. As an example, the cases at $\delta = 0.05$ for $1 < \lambda < 2$ present a remarkable difference in α and ω, so on the modes found, but the same cannot be said for $\delta = 0.03$, despite the fact that both present relevant differences in Re_{cr}. The neutral curves for Re_{cr} are continuous, but they present a sharp change when, increasing the torsion, the symmetric mode stops to prevail (so-called change of stability). Another important aspect is that critical Reynolds numbers are generally monotonically decreasing with torsion, except for high curvatures and torsions. This finding suggests that the torsion generally has a destabilising effect. However, for high values of τ, the basic state resembles the flow in a straight pipe flow with swirl, thus the critical Reynolds number increases, due to the divergence of R_{cr} for straight pipes.

Figure 11 shows the streamwise wavenumber α of the marginally stable modes, whereas their frequency ω is reported in Figure 10. The agreement with Gelfgat (2020) is again quite good, except for a few combinations (δ, τ). A remarkable difference is observed in the frequency for $\delta = 0.2$ and $\lambda \approx 2.1$, since a novel family of unstable modes, not found by Gelfgat (2020), is identified.

Mode coexistence

The jumps along the global neutral curves for ω and α occur when different families of critical modes interchange with each other as λ varies. An example of this behaviour can be observed, for example, for $\delta = 0.05$ and $\lambda \approx 1$. The neutral curves (Re_{cr}, α) displayed in Figure 12 show that there exist two families of modes (mode 5 and mode 6, described in Casali (2025)) that become unstable for similar values of the Reynolds number, with mode 6 being the critical one for $\lambda \geq 1$. Decreasing λ, Re_{cr} for mode 5 is reduced, while Re_{cr} for mode 6 increases. Hence, there is a value of λ for which both families coexist at criticality, with mode 5 becoming the critical one for $\lambda < 1$.

It must be pointed out that the modal stability analysis does not consider the interaction between different modes. Because of the non-orthogonality of the eigenmodes, these interactions can give rise to a transient energy growth, which can cause transition to turbulence if a certain energy threshold is exceeded (Schmid & Henningson (2001)).

CONCLUSIONS

We report on our studies of the flow in helical pipes, fully-developed in the streamwise direction such that periodic boundary conditions can be applied. We start with analysing the laminar steady base flow, where the specific pressure gradient to drive the flow is validated against inflow–outflow configurations. It is further shown that the amplitude of the secondary flow, and the related Darcy friction factor, is varying non-monotonically as function of the torsion and curvature of the helical pipe. Moving towards flow instability, we extensively validate our 2D stability code that is able to compute eigenvalues and neutral curves for any parameters of the helical configuration. We compare our stability results to literature data by Gelfgat (2020), and find generally good agreement, with some differences being highlighted.

Further work on helical pipe would include a characterisation of the actual transition process, potentially comparing to the interesting critical points identified by Canton *et al.* (2020) in toroidal flows. Also, the relevance of transient growth in any of the helical or toroidal configurations has not yet been studied. Finally, the turbulent flow in a helical pipe, modulated by the secondary flow, is clearly relevant, but essentially unstudied at higher Reynolds numbers.

REFERENCES

Avila, M., Barkley, D. & Hof, B. 2023 Transition to turbulence in pipe flow. *Annual Review of Fluid Mechanics* **55**, 575–602.

Canton, J., Örlü, R. & Schlatter, P. 2017 Characterisation of the steady, laminar incompressible flow in toroidal pipes covering the entire curvature range. *International Journal of Heat and Fluid Flow* **66**, 95–107.

Canton, J., Rinaldi, E., Örlü, R. & Schlatter, P. 2020 Critical point for bifurcation cascades and featureless turbulence. *Physical Review Letters* **124** (1), 014501.

Canton, J., Schlatter, P. & Örlü, R. 2016 Modal instability of the flow in a toroidal pipe. *Journal of Fluid Mechanics* **792**, 894–909.

Casali, R. 2025 Laminar flow and linear stability in helical pipes. Master's thesis, Università di Bologna, Bologna, Italy.

Dean, W. R. 1927 Note on the motion of fluid in a curved pipe. *The London, Edinburgh, and Dublin Philosophical Magazine and Journal of Science* **4** (20), 208–223.

Drazin, P. G. & Reid, W. H. 2004 *Hydrodynamic Stability*. Cambridge University Press.

Fischer, P. F., Lottes, J. W. & Kerkemeier, S. G. 2025 nek5000 Web page. Https://nek5000.mcs.anl.gov.

Gelfgat, A. 2020 Instability of steady flows in helical pipes. *Physical Review Fluids* **5** (10), 103904.

Germano, M. 1982 On the effect of torsion on a helical pipe flow. *Journal of Fluid Mechanics* **125**, 1–8.

Hüttl, T. J., Wagner, C. & Friedrich, R. 1999 Navier–Stokes solutions of laminar flows based on orthogonal helical coordinates. *International Journal for Numerical Methods in Fluids* **29** (7), 749–763.

Jansson, N., Karp, M., Podobas, A., Markidis, S. & Schlatter, P. 2024 Neko: A modern, portable, and scalable framework for high-fidelity computational fluid dynamics. *Computers & Fluids* **275**, 106243.

Kumar, A. 2020 Pressure-driven flows in helical pipes: bounds on flow rate and friction factor. *Journal of Fluid Mechanics* **904**, A5.

Lupi, V., Canton, J., Rinaldi, E., Örlü, R. & Schlatter, P. 2024 Modal stability analysis of toroidal pipe flow approaching zero curvature. *Journal of Fluid Mechanics* **987**, A40.

Schmid, P. J. & Henningson, D. S. 2001 *Stability and Transition in Shear Flows*. Springer New York.